All differences between the curves' shapes described above evince the aptitude of TPA to form dense and uniform AAO with well-expressed barrier properties, whereas the AA2024-T3 forms an oxide layer which does not protect the alloy efficiently.

The LVA curves, acquired after 168 hours of exposure for all investigated samples were submitted to further Tafel slope analysis and the results are shown in Table 2.

The corrosion potential (E_{corr}) values of the alloy samples are in a very narrow interval between -618 and -634 mV, (measured vs. Ag/AgCl/3M KCl), whereas a great E_{corr} dissipation was registered for the pure aluminum. The mentioned E_{corr} deviations for TPA are a result of the insignificant current densities (approaching the equipment detection minimum threshold). The R_p values for TPA are by two orders of magnitude higher than those for AA2024-T3. This fact is an additional evidence for the superior barrier properties of the AAO, formed on the technically pure aluminum.

Table1. EIS data fitting results from the spectra acquired after 168 hours of exposure

Anodized TPA samples					
Element	Unit		Sample **1**	Sample **2**	Sample **3**
R_{el}	$\Omega\ cm^2$		28.24 ± 3.08	50.74 ± 6.78	50.04 ± 4.90
C_{oxy}	$\mu F\ cm^{-2}$		1.50 ± 0.12	0.760 ± 0.10	1.40 ± 1.40
R_{oxy}	$\Omega\ cm^2$	10^3	1.568 ± 0.76	0.29 ± 0.06	3.08 ± 0.80
C_{edl}	$\mu F\ cm^{-2}$		0.685 ± 0.01	0.570 ± 0.01	0.70 ± 0.01
R_{ct}	$\Omega\ cm^2$	10^6	102.80 ± 28.26	120.40 ± 38.44	286.40 ± 274.54
Anodized AA2024-T3 alloy					
Element	Unit		Sample **1**	Sample **2**	Sample **3**
R_{el}	$\Omega\ cm^2$		16.04 ± 0.73	40.38 ± 2.85	14.42 ± 0.76
Q_{oxy1}	$s^n\Omega^{-1}cm^{-2}$	10^{-6}	4.23 ± 0.49	27.78 ± 6.00	48.04 ± 1.84
n	-		0.88 ± 0.03	1.00 ± 0.09	0.96 ± 0.02
R_{oxy1}	$\Omega\ cm^2$	10^3	0.85 ± 0.13	51.78 ± 12.32	12.16 ± 1.34
Q_{oxy2}	$s^n\Omega^{-1}cm^{-2}$	10^{-6}	7.78 ± 0.51	4.31 ± 0.19	7.30 ± 1.22
n	-		0.77 ± 0.01	1.00 ± 0.03	0.95 ± 0.04
R_{oxy2}	$\Omega\ cm^2$	10^3	71.00 ± 15.14	31.50 ± 5.05	0.48 ± 0.06
Q_{edl}	$s^n\Omega^{-1}cm^{-2}$	10^{-6}	14.78 ± 2.50	19.62 ± 3.10	27.25 ± 2.28
n	-		0.96 ± 0.03	0.60 ± 0.15	0.65 ± 0.07
R_{ct}	$\Omega\ cm^2$	10^3	161.00 ± 16.09	109.60 ± 14.61	40.80 ± 1.08

Table 2. Tafel plot analysis of the polarization curves acquired after 168 hours of exposure

	Cathodic curves R_p ($k\Omega\ cm^2$)		Anodic curves R_p ($k\Omega\ cm^2$)	
Sample	**TPA**	**AA 2024**	**TPA**	**AA 2024**
S 1	$22.90x10^3$	192.08	$26.76x10^3$	192.26
S 2	$23.32x10^3$	161.90	$40.14x10^3$	157.30
S 3	$51.10x10^3$	41.72	$37.60x10^3$	45.90

The corrosion potential (E_{corr}) values of the alloy samples are in a very narrow interval between -618 and -634 mV, (measured vs. Ag/AgCl/3M KCl), whereas a great E_{corr} dissipation was registered for the pure aluminum. The mentioned E_{corr} deviations for TPA are a result of the insignificant current densities (approaching the equipment detection minimum threshold). The R_p values for TPA are by two orders of magnitude higher than those for AA2024-T3. This fact is an additional evidence for the superior barrier properties of the AAO, formed on the technically pure aluminum.

Impact of the anodization process on the surface morphology

Scanning Electron Microscopy

The SEM images (Fig. 5) reveal that the impact of the anodization process for the technically pure aluminum and the highly doped

AA2024-T3 differs. In the former case, the AAO film repeats the substrate's topology. It can be described as laminar surface (inset of position (a)) with multitude of pits (position (a) basic image). The laminar surface is obtained during the Al-foil rolling, whereas the pits are formed during the preliminary etching and acid activation.

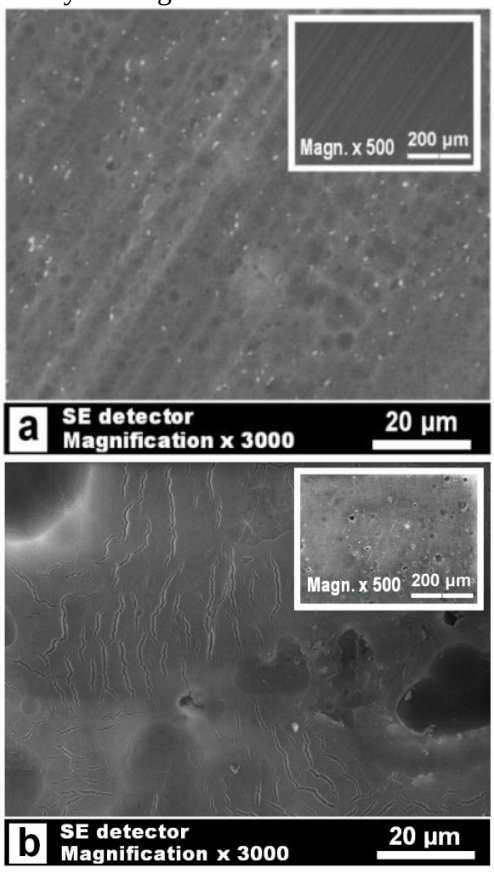

Fig. 5. SEM images of the investigated samples: (a) TPA and (b) AA2024-T3

The AAO layer, formed on AA2024-T3 is covered by multitude of cracks and ruptures. In addition, in the inset of position (b) a large number of wide caverns (not pits) are observable. The results of previous research works dedicated on the preliminary treatment of this alloy [31-33] lead to the inference that these concavities are rather result of the sample etching and acidic activation than to be consequence of the anodization process. These observations completely correlate with the EIS data analysis results. Probably, the cracks and ruptures, together with the entrapped electrolyte correspond to (CPE_{oxy1} R_{oxy1}), whereas the time constant (CPE_{oxy2} R_{oxy2}) shows that these defects do not reach the metallic surface, hence a denser inner oxide layer is present.

Atomic Force Microscopy

The AFM images (Fig. 6) reveal that in the case of TPA, the AAO film repeats the substrate's topology. Consequently, the anodization of the technically pure aluminum results in only slight smoothening of the laminas and increase of the pits' number and depth.

For comparison, the AA2024-T3 surface looks rather different from the above described even prior to anodization. Besides the cracks commented above (regarding the SEM images), wide caverns instead of pits are observable for the alloy samples. Also, coarse formations are observable, probably due to occurrence of large-sized intermetallics, which are formed during the thermal treatment of the alloy.

The formation of pits and caverns during the preliminary treatments (etching and acidic activation) can be ascribed to selective dissolution phenomena. These phenomena involve the smaller grains in the case of TPA and adjacent Al-matrix surrounding the cathodic intermetallics of the AA2024-T3 alloy, respectively.

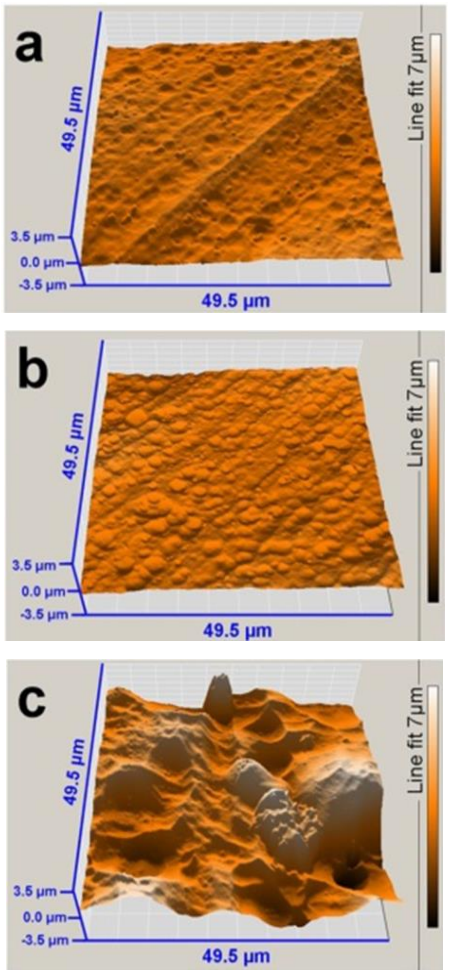

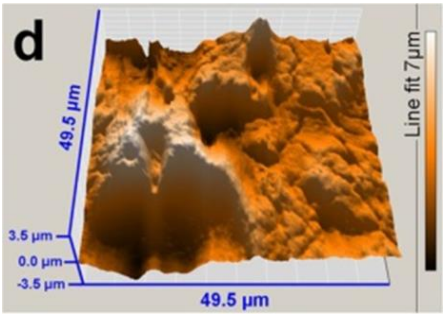

Fig. 6. AFM images of reference (a, c) and anodized (b, d) samples of TPA (a, b) and AA2024-T3 (c, d)

The quantitative AFM data analysis for TPA causes surface roughness increment, regarding the roughness mean (S_m) from 0.4 to 31.2 pm. This S_m increase (of almost 80 times) confirms the inference for pit depth and number increase during the anodization.

For comparison, the anodization of AA2024 leads to greater topological changes than in the case of TPA. The AAO film formed on the alloy shows that the anodization results in twice rougher topology (S_m values from 62.8 pm for TPA up to 190.1 pm for AA2024). This difference can be explained, considering the coincidence of Al-oxide film growth and selective dissolution around the intermetallics.

The maximal distance between the highest and the lowest points (S_y) for TPA changes from S_y = 1.50 to 1.31 µm, due to the anodization process. This S_y decrement with about 0.30 µm is consequence of the smoothening of the laminar ridges, which cannot be compensated by the pitting proliferation, discussed above. For comparison, the AA2024-T3 samples preserve their topology with negligible decrease of S_y from 6.40 to 6.14 µm, regarding the total roughness.

CONCLUSIONS

The in-situ chronopotentiometric curves of TPA possess a sharp initial rise (until 22.5 V), whereas for AA2024-T3 alloy, there is retention of about 30-40 s at 5 V. This phenomenon is related to the differences of the initial oxide layers, formed on TPA foil and AA2024-T3 alloy during the preliminary treatment procedures. The occurrence of the potential retention at 5 V is probably related either to Cu-intermetallics oxidation, or to adjacent Al matrix oxide layer growth, coinciding the intermetallics dissolution. Besides, the horizontal parts of TPA are slightly lower, compared to those for the alloy. This fact is a result of the higher roughness, resulting from the intermetallics selective dissolution during the preliminary treatment procedures.

The TPA samples needed EIS data acquisition at a much higher excitation signal amplitude, in order to obtain readable spectra. The rather distinguishable EIS spectra shapes for the pure aluminum and the alloy reveal clear structural differences of the AAO films, as consequence of the respective substrate compositions. These rather different spectra shapes required different equivalent circuits for quantitative data fitting analysis. The analysis results have shown purely capacitive properties of the AAO formed on TPA, whereas the alloy showed irregular oxide layer, due to intermetallic occurrence.

The cathodic curves for TPA are almost horizontal, due to the barrier passivation of AAO film, whereas the respective curves acquired for the AA2024-T3 alloy are smooth and reveal clear occurrence of corrosion processes. Similar trends are observable for the respective anodic curves. Besides, the anodic curves of the alloy possess inflexions, revealing localized corrosion activity. The polarization resistance (R_p) values for TPA are by two orders of magnitude higher than those for AA2024-T3, because of the superior barrier properties of the AAO, formed on the technically pure aluminum. The corrosion potential (E_{corr}) values of the alloy samples are in a very narrow interval, but a great E_{corr} dissipation was registered for TPA as a result of the random pit distribution, as well as the insignificant current densities, near to the equipment detection minimum threshold.

The SEM and AFM images reveal that the impact of the anodization process for the technically pure Al and the highly doped AA2024-T3 is quite different. In the former case, the anodization results in only slight smoothening of the laminas and increase of the pits' number and depth. The AA2024-T3 surface looks rather different from the above described even prior to anodization. Wide caverns instead of pits are observable for the alloy samples. Besides, coarse formations are also observable, probably due to occurrence of large size intermetallics, which are formed during the thermal treatment of the alloy. The formation of pits and caverns during the preliminary treatments can be ascribed to selective dissolution of smaller grains of the TPA, and adjacent Al-matrix surrounding the cathodic intermetallics of the AA2024-T3 alloy, respectively. Its AAO film has a more distinguishable topology, compared to the respective bare alloy. The quantitative AFM data analysis shows that the AAO film is twice smoother for TPA, than the bare AA2024-T3 alloy (with S_m values of 190.10 to 62.8 pm), because of

coincidence of Al-oxide film growth and selective dissolution.

Summarizing the results of the electrochemical measurements and the topological observations, it can be inferred that the TPA forms uniform AAO, whereas the oxide layer on AA2024-T3 is composed by a cracked outer layer and an underlayer.

***Acknowledgements**: The funding of this work under contract DFNI-T02–27 by the Bulgarian National Scientific Research Fund is highly appreciated.*

REFERENCES

1. J. Siejka, C. Orteg, *J. Electrochem. Soc*. **124**, 883 (1977).
2. V.P. Parkhutik, J. M. Albella, Yu. E. Makushok, I. Montero, J.M. Martinez-Duart, V.I. Shershulskii, *Electrochim. Acta*, **35**, 955 (1990).
3. V.P. Parkhutik, V.T. Belov, M.A. Chernyckh, *Electrochim. Acta*, **35**, 961 (1990).
4. Ch. Girginov, S. Kozhukharov, *Internat. J. Electrochem.* (2011), Article ID 126726; doi:10.4061/2011/126726
5. V. Surganov. C. Jansson. J.G. Nielsen. P. Morgen, *Electrochim. Acta*, **33**, 517 (1988).
6. K.V. Heber, Electrochim. Acta 23, 127 (1978).
7. K.V. Heber, *Electrochim. Acta*, **23**, 135 (1978).
8. F. Nasirpouri, M. Abdollahzadeh, M.J. Almasi, N. Parvini-Ahmadi, *Current Appl. Phys.*, **9**, S91 (2009).
9. A. Bai, C-C.Hu, Y-F.Yang, C-C. Lin, *Electrochim. Acta*, **53**, 2258 (2008).
10. C-U. Yu, C-C.Hu, A. Bai, Y-F. Yang, *Surf. Coat. Tech.*, **201**, 7259 (2007).
11. J.M. Montero-Moreno, M. Sarret, C. Müller, *Surf. Coat. Tech.*, **201**, 6352 (2007).
12. S. Ono, M. Saito, H. Asoh, *Electrochim. Acta*, **51**, 827 (2005).
13. M. Ghorbani, F. Nasirpour , A. Iraji-zad, A. Saedi, *Materials & Design*, **27**, 983 (2006).
14. W. J. Stępniowski, M. Salerno, Chapter 12. Fabrication of nanowires and nanotubes by anodic alumina template-assisted electrodeposition, Manufacturing Nanostructures (Eds. Waqar Ahmed, Nasar Ali), One Central Press (2014) pp. 321-357.
15. E. A. Starke, Jr., J. T. Staley, Prog. Aerospace Sci., 32, 131 (1996).
16. S. V. Kozhukharov, Deposition of Environmentally Compliant Cerium-Containing Coatings and Primers on Copper-Containing Aluminium Aircraft Alloys, Biobased and Environmental Benign Coatings (eds A. Tiwari, A. Galanis and M. D. Soucek), John Wiley & Sons, Inc. (2016), Hoboken, NJ, USA. p. 20
17. F.M. Queiroz, M. Magnani, I. Costa, H.G. de Melo, *Corr. Sci.*, **50**, 2646 (2008).
18. Ch. Blanc, G. Mankowski, *Corr. Sci*., **40**, 411 (1998).
19. J.A. DeRose, T. Suter, A. Bałkowiec, J. Michalski, K.J. Kurzydlowski, P. Schmutz, *Corr. Sci.*, **55**, 313 (2012).
20. A. Aballe, M. Bethencourt, FJ. Botana, M. Marcos, M.A. Rodríguez-Chacón, *Rev. Metal.*, **34**, 42 (1998).
21. V. Guillaumin, G. Mankowski, *Corr. Sci*. **41**, 421 (1998).
22. A. Boag, R.J. Taylor, T.H. Muster, N. Goodman, D. McCulloch, C. Ryan, B. Rout, D. Jamieson, A.E. Hughes, *Corr. Sci*., **52**, 90 (2010).
23. A. E. Hughes, C. MacRae, N. Wilson, A. Torpy, H. T. Muster, A. M. Glenn, Surf. *Int. Anal.*, **42**, 334 (2010).
24. C. Blanc, B. Lavelle, G. Mankowski, *Corr. Sci.*, **39**, 495 (1997).
25. S. Kozhukharov, M. Milanes, C. Girginov, M. Machkova, *Materials and Corrosion*, DOI: 10.1002/maco.201508635
26. M. Zaki-Mubarok, W. Sutarno, S. Wahyudi, *J. Min. Mater. Char. Eng*., **3**, 154 (2015).
27. G. Boisier, N. Pébère,a, C. Druez, M. Villatte, S. Suelb, *J. Electrochem. Soc*., **155**, C521 (2008).
28. M. Xiangfeng, W. Guoying, G. Hongliang, Y. Yundan, C. Ying, H. Dettinger, *Int. J. Electrochem. Sci.*, **8**, 10660 (2013).
29. S. Kozhukharov, Ch. Girginov, I. Avramov, M. Machkova, *Mat. Chem. Phys.*, **180**, 301 (2016).
30. M. Curioni, P. Skeldon, E. Koroleva, G. E. Thompson, J. Ferguson, *J. Electrochem. Soc.*, **156**, C147 (2009).
31. E. A. Matter, S. Kozhukharov, M. Machkova, V. Kozhukharov, *J. Chem. Tech. Metall*., **50**, 52 (2015).
32. E. A. Matter, S. V. Kozhukharov, M. S. Machkova, *Bul. Chem. Comm.*, **43**, 23 (2011).
33. E. Matter, S. Kozhukharov, *Ann. proceed. Univ. Rousse (Bulgaria),* **49**, 14 (2010).
34. M. Bethencourt, F.J. Botana, J.J. Calvino, M. Marcos, M.A. Rodriguez-Chacon, *Corr. Sci.*, **40**, 1803 (1998).

СРАВНИТЕЛНО ЕЛЕКТРОХИМИЧНО И ТОПОЛОГИЧНО ИЗСЛЕДВАНЕ НА АНОДНИ ОКСИДНИ ФИЛМИ ФОРМИРАНИ ВЪРХУ ТЕХНИЧЕСКИ ЧИСТ АЛУМИНИЙ И САМОЛЕТНА AA2024-T3 СПЛАВ

С. В. Кожухаров, К. А. Гиргинов

Химикотехнологичен и металургичен университет, бул. Климент Охридски № 8, 1756 София (България)

Постъпила на 28 юни 2017 г.; приета на 07 октомври 2017 г.

(Резюме)

Големите разлики в механичните свойства на чистия алуминий и неговите индустриални сплави предопределя значителни вариации на тяхното химично и електрохимично поведение. Този факт налага по-подробно изследване на връзката между състава на сплавта и нейното отнасяне при предварителните химични обработки, както и при излагане в корозионни среди. Настоящото изследване е посветено на сравнението на анодните оксидни филми (AAO), формирани при еднакви условия върху технически алуминий (TPA) и високо легирана сплав (AA2024-T3). Анодирането е провеждано в галваностатично-изотермичен режим, като са регистрирани in-situ хроно-потенциометрични кинетични криви. Електрохимичното поведение на анодираните образци в 3.5% NaCl среда е изследвано чрез електрохимична импедансна спектроскопия (EIS) и линейна волтаметрия (LVA). Топологията на формираните AAO филми е наблюдавана чрез сканираща електронна микроскопия (SEM) и атомно-силова микроскопия (AFM). Чрез използваните аналитични техники е установена забележима разлика в отнасянията на AAO-филмите, образувани върху TPA и тези върху AA2024-T3. Използваните електрохимични методи показаха напълно различни отнасяния, което е потвърдено и от извършения допълнителният цифров анализ на експерименталните данни. Повърхностните наблюдения (SEM и AFM) разкриха напълно различна топологична картина на повърхността за двата изследвани алуминиеви състава. От обобщението на резултатите от електрохимичните измервания и топологичните наблюдения, може да се заключи, че TPA образува равномерен AAO филм, докато оксидният слой върху AA2024-T3 е по-скоро напукан и притежава по-малка трайност в моделната корозивна среда.

Ключови думи: анодиране на алуминий, AA2024-T3, EIS, LVA, SEM, AFM